Journal of Materials Chemistry A

Local Structure Analysis and Structure Mining for Design of Photocatalytic Metal Oxychloride Intergrowths

Journal:	*Journal of Materials Chemistry A*
Manuscript ID	TA-ART-07-2022-005663.R1
Article Type:	Paper
Date Submitted by the Author:	15-Sep-2022
Complete List of Authors:	Chatterjee, Kaustav; Indiana University Bloomington, Dept. of Chemistry Magnard, Nicolas ; Kobenhavns Universitet, Dept. of Chemistry Mathiesen , Jette ; University of Copenhagen, Nanoscience Center & Department of Chemistry Jensen, Kirsten Marie; Kobenhavns Universitet, Dept. of Chemistry; Skrabalak, Sara; Indiana University - Bloomington, Chemistry

ARTICLE

Local Structure Analysis and Structure Mining for Design of Photocatalytic Metal Oxychloride Intergrowths

Received 00th January 20xx,
Accepted 00th January 20xx

DOI: 10.1039/x0xx00000x

Kaustav Chatterjee,[a‡] Nicolas Pierre Louis Magnard,[b‡] Jette K. Mathiesen,[c‡] Kirsten M. Ø. Jensen,*[b] and and Sara E. Skrabalak,*[a]

In this work, the local structures of durable, high-activity Bi_4TaO_8Cl–Bi_2GdO_4Cl intergrowth photocatalysts that were prepared in a molten flux are determined by pair distribution function analysis of X-ray total scattering data and correlated to their photocatalytic performance. This system gives understanding to how the local structure of photocatalysts can be manipulated controllably through incorporation of rigid and flexible layers *via* intergrowth formation to achieve high activity. This analysis revealed that the local symmetry and distortion of the [TaO_6] octahedra introduced through intergrowth formation and dictated by intergrowth stoichiometry correlate with their photocatalytic activity. That is, the greater the Ta–O–Ta bond angles, the higher the photocatalytic activity of a given intergrowth for the oxygen evolution reaction. Moreover, greater tilting of the [TaO_6] octahedra is associated with a larger band gap. This analysis was coupled with a structure mining approach to model the intergrowth structure by building supercells for refinement of the X-ray diffraction data. This analysis found that Ta- and Gd-domains are separated within the intergrowths, with large Gd-domains separated by small Ta-domains at high Gd% and the opposite for high Ta%. Taken together with Williamson-Hall analysis, our results highlight that the local structure of layered materials can be modulated through strain engineering enabled by the selection of rigid and flexible intergrowth layers, providing a new design pathway to high performance photocatalysts.

1. Introduction

Sunlight driven photocatalytic water splitting is a potentially transformative renewable-energy technology.[1,2] Although heterogeneous semiconductor-based photocatalysts have been extensively studied, how local structural variations contribute to key properties and can be intentionally manipulated remain understudied because of the complex reaction process and complex materials used as photocatalysts.[3–6] Yet, determination of structure–property relationships is essential to advancing the field.[7,8] Traditional photocatalysts are metal oxides containing d^0 or d^{10} transition metals, but owing to their large band gaps, these materials cannot harvest visible-light of the solar spectrum.[9,10] Bismuth-based oxyhalide materials of the type Bi_4MO_8X (M=Ta, Nb; X=Cl, Br) have potential as durable photocatalysts with visible-light irradiation.[11–14] These phases are composed of alternating layers of perovskite $[MO_4]^{3-}$, halide $[X]^-$, and two $[Bi_2O_2]^{2+}$ blocks. Excitingly, introducing additional metal perovskite slabs or atom substitutions can tune their optoelectronic properties over a broad range.[15–17] Here, the structural origins of such tunable properties are elucidated for recently reported visible-light-responsive and durable Bi_4TaO_8Cl–Bi_2GdO_4Cl intergrowths, giving guidance for the design of new photocatalytic materials.[16,18]

Intergrowths are layered materials formed from two different crystal structures by stacking of layers on top of each other.[19] Depending on the order of stacking, either ordered or disordered intergrowths are possible.[20] Compared to hetero/phase junction materials which consist of two different materials, intergrowths are compound crystal phases with elemental homogeneity at the nanoscale. The study of intergrowths for photocatalysis is attractive given their modular nature, where different layers can be selected to facilitate crystal structure engineering and, in turn, electronic structure engineering. Additionally, through such crystal structure engineering, the inter-layer electrostatic interaction of intergrowths can be tuned towards facile separation of electrons and holes. These benefits motivate the further study of the recently reported Bi_4TaO_8Cl–Bi_2GdO_4Cl intergrowths given their high activity for visible-light-driven water splitting.

The Bi_4TaO_8Cl–Bi_2GdO_4Cl intergrowths were synthesized in a molten flux and prior characterization found them to be disordered,[16] although a schematic structure of the 1:1 Ta:Gd Bi_4TaO_8Cl–Bi_2GdO_4Cl intergrowth shown in **Figure 1a** depicts an ordered intergrowth to clearly represent the building block layers. Prior characterization also found the band gaps of the intergrowths to depend on the Ta:Gd molar ratio, and overall water splitting using a Z-scheme was achieved with high material durability. In this report, the local structures of these previously synthesized Bi_4TaO_8Cl–Bi_2GdO_4Cl intergrowths are

[a] *Department of Chemistry, Indiana University—Bloomington, Bloomington, Indiana 47405, United States.*
[b] *Department of Chemistry, University of Copenhagen, DK-2100 Copenhagen, Denmark.*
[c] *Department of Physics, Technical University of Denmark, DK-2800 Kgs. Lyngby, Denmark*
Electronic Supplementary Information (ESI) available: See DOI: 10.1039/x0xx00000x
‡ These authors contributed equally to this work.

elucidated and correlated with photocatalytic performance. The local structure of these intergrowths are interesting to study as the [TaO_6] octahedra within the Bi_4TaO_8Cl layers can distort/tilt while the GdO_8 in cubic geometry are more rigid, making these intergrowths suitable for a systematic structural study. That is, these qualities allow the Ta−O−Ta bond angle and tilt of [TaO_6] to be varied systematically as a function of intergrowth composition for elucidation of how these features contribute to photocatalytic activity and, more broadly, how the local structure of photocatalysts can be controllably manipulated through intergrowth formation for enhanced performance.

Studies that correlate the local structure of a material to fundamental processes relevant to photocatalysis are of high value, with their results guiding design of future materials. For example, a comparison of $Sr_2Ta_2O_7$ and $Sr_2Nb_2O_7$ correlated the superior photocatalytic activity of $Sr_2Ta_2O_7$ to greater electron-hole mobility, arising from the higher degree of linearity for the Ta−O−Ta bonds that comprise the corner-shared octahedra of this material compared to the Nb−O−Nb bonds in the latter.[21] In a related study, $ATaO_2N$ (A = Ca, Sr, Ba) were evaluated as photocatalysts and the band gap energy was found to decrease with a decrease in octahedral tilting, largely through modification of the conduction band energy of these materials.[22] Considering the systems that comprise the intergrowths studied here, Bhat *et al.* also found through the use of powder neutron Rietveld refinement, neutron pair distribution function (PDF) analysis, Raman scattering, and density functional theory calculations that the performance of Bi_4TaO_8Cl depends on Ta−O−Ta bond angle and octahedral tilt. Specifically, nanoscale Bi_4TaO_8Cl was found to be superior to bulk Bi_4TaO_8Cl, which was attributed to size-dependent structural distortions that increased octahedral tilting and decreased Ta−O−Ta bond angles.

In contrast to these prior studies, we prepared Bi_4TaO_8Cl–Bi_2GdO_4Cl intergrowths with different Ta:Gd ratios and report here their local structures in comparison to the parent phases. This analysis reveals how intergrowth formation and the incorporation of rigid *versus* flexible layers modulates the local structure of the photocatalyst. In turn, the local structure features are correlated to the performance of these intergrowths as photocatalysts for the oxygen evolution reaction (OER). This analysis is coupled with a structure mining approach to model the intergrowth structure. Taken together with Williamson-Hall analysis, our results highlight that the local structure of layered materials can be modulated through strain engineering enabled by the selection of rigid and flexible intergrowth layers, providing a new design pathway to high performance photocatalysts.

2. Experimental Section

2.1 Reagents and Materials

Bismuth(III) oxide (Bi_2O_3, Sigma-Aldrich, 99.99%), tantalum(V) oxide (Ta_2O_5, Sigma-Aldrich, 99.9%), bismuth chloride oxide (BiOCl, Alfa-Aesar, 98%), gadolinium oxide (Gd_2O_3, Alfa-Aesar, 99.9%), sodium chloride (NaCl, Sigma-Aldrich, >99%), caesium chloride (CsCl, Sigma-Aldrich, 99.9%) and acetone (C_3H_6O, Macron, ACS grade) were used as received without further purification. Nanopure water was used in all the experiments as required having a resistivity of 18.2 MΩ cm at 25 °C.

2.2 Synthesis of Bi_4TaO_8Cl–Bi_2GdO_4Cl Intergrowths and pristine Bi_4TaO_8Cl and Bi_2GdO_4Cl

Samples previously reported were used for the advanced characterization described herein. The details of their synthesis are provided again for clarity.[16]

Pristine Bi_4TaO_8Cl (Ta 100%): Stoichiometric quantities of Bi_2O_3, Ta_2O_5, and BiOCl (3:1:2) powders were weighed and then grounded to a homogeneous mixture in a mortar and pestle (Agate), and then the resulting powder was transferred to an alumina crucible. The crucible was heated in a tube furnace at 700 °C for 12 under N_2 (flow rate 20 mL/min).

Pristine Bi_2GdO_4Cl (Ta 0%): Stoichiometric quantities of Bi_2O_3, Gd_2O_3, and BiOCl (1:1:2.4) powders were weighed and then grounded to a homogeneous mixture in a mortar and pestle (Agate), and then the resulting powder was transferred to an alumina crucible. The crucible was heated at 800 °C for 4 h under N_2 (flow rate 20 mL/min).

Intergrowth samples (Ta 25%, Ta 50% and Ta 75%): Intergrowth samples were synthesized by molten flux synthesis. The eutectic mixture salt of CsCl/NaCl (65:35) was used as flux. The flux was mixed with stoichiometric quantities of Bi_2O_3, Ta_2O_5, Gd_2O_3, and BiOCl at a solute concentration [Bi_4TaO_8Cl–Bi_2GdO_4Cl/(Bi_4TaO_8Cl–Bi_2GdO_4Cl + flux)] of 5 mol %. The mixture was grinded to a homogeneous powder and transferred to an alumina crucible. The crucible was heated at 700 °C for 12 h under N_2 (flow rate 20 mL/min) at a rate of 7.5 °C min^{-1}. Different intergrowth samples were prepared varying the molar ratio of Ta_2O_5 and Gd_2O_3. After natural cooling, the product was thoroughly washed and centrifuged with nanopure water and ethanol/acetone (1:1) mixture. The obtained powder samples were dried overnight under vacuum at room temperature.

All the synthesized samples were used for further analysis as is and without further modifications. The intergrowth samples are named as Ta *X* %, where *X* denotes the relative percentage of Bi_4TaO_8Cl in the Bi_4TaO_8Cl–Bi_2GdO_4Cl intergrowth phases with respect to the initial Ta_2O_5/Gd_2O_3 molar ratio.

The prepared samples were characterized by Field Emission Scanning Electron Microscope (FESEM). FESEM was performed on a FEI Quanta 600F operated at 30 kV. Energy Dispersive X-ray Spectroscopy (EDS) measurements was carried with an Oxford Inca detector operating at 10 kV. Samples for SEM-EDS were prepared by drop-casting approximately 2 µL of a dispersed sample in ethanol onto a silicon wafer and let dry.

2.3 Powder X-ray Diffraction (PXRD), X-ray Total Scattering (TS) and PDF analysis

***Data acquisition*.** The *ex situ* PXRD and X-ray TS data were obtained at beamline 11-ID-B, Advanced Photon Source (APS) Argonne National Laboratory, USA. The intergrowth samples

were loaded into a Kapton capillary with an outside diameter of 1.05 mm and a wall thickness of 0.025 mm. *Ex situ* PXRD and TS data were collected in transmission geometry using a Perkin-Elmer detector with a pixel size of 200×200 µm and a wavelength of 0.2115 Å. The sample-to-detector distance and instrumental parameters (Q_{broad}=0.039 Å^{-1} and Q_{damp}=0.017 Å^{-1}) were calibrated using a CeO_2 standard. *Fit2D* was used to calibrate the experimental geometry parameters and azimuthally integrate the scattering intensities to 1D scattering patterns.[23,24]

***PDF modelling*.** Experimentally obtained X-ray TS data were Fourier transformed through *xPDFsuite* to obtain the PDFs using a Q_{min} of 0.8 Å^{-1} and a Q_{max} of 25.0 Å^{-1}.[25] To isolate the structural information of interest, a background correction was performed by subtracting the scattering signal of an empty Kapton capillary. Modelling of the experimental PDFs was done using *PDFgui*, in which a least-square optimization procedure was performed between a theoretical PDF and the experimental PDF.[26] The refined parameters included the unit cell, δ_2-parameter describing local correlated atomic movement, scale factor, a spherical particle diameter, the atomic positions of Ta and Bi, and the isotropic atomic displacement parameters for the atoms in the given structures. The atomic positions were constrained from the space group symmetry of the parent phases.

2.4 Structure mining

Simulated supercells containing various amount of intergrowth of Gd- and Ta-domains were created to be able to compare calculated XRD patterns and PDFs to experimental data through structure mining. The methodology for creating supercells for structure mining has been described in detail in previous work.[27] Briefly, as further discussed below, asymmetric units of the Ta- and the Gd-domains were extracted and stacked sequentially following a set of probabilities P_g and P_t. 50 units were stacked in total. The simulated PXRD patterns of the supercells were modelled and refined against the experimental PXRD datasets using Rietveld refinement. The refinements were performed in *Topas Academic* and cell parameters of the supercell, thermal atomic displacement, a background function using a Chebyshev polynomials with 9 parameters and a TCHZ peak shape were refined.[28] Single peak fitting was also performed using *Topas Academic* for the building of Williamson-Hall plots. A Pseudo-Voigt function was fitted to each diffraction peak and its Full Width at Half Maximum was extracted.

3. Results and Discussion

3.1 PDF Analysis

As previously reported through Rietveld analysis of PXRD data, the intergrowth structure can be described by a two-phase model with the metal positions provided by the parent phases.[16] We adopted a similar two-phase model when investigating the local structure using TS and PDF analysis of the parent and intergrown phases as presented in **Figure 1**. An indication of the quality of the PDF refinement is provided through the parameter R_{wp}, where a lower R_{wp} indicates a better agreement between the experimental data and model used for the fit. As observed in **Figure 1b**, the two-phase refinements yield low R_{wp} values, which indicate a high degree of resemblance between the models and data. The phase fractions in **Figure 1c**, top, show that the intended fractions of the two structures in the intergrowth have been achieved by our synthesis protocol (slight deviations in phase fractions could be noticed which can be attributed to the loss metal precursors or unavoidable of decomposition of some intermediates during the molten-flux reaction). The experimentally obtained atomic ratios of the samples by SEM-EDS is listed in **Table S1**.

To evaluate the impact of intergrowth formation on the two parent unit cells (Bi_4TaO_8Cl- Ta 100% and Bi_2GdO_4Cl- Ta 0%), the lattice parameters of the two phases were extracted from the refinement analysis. **Figure 1c** (bottom) shows the *c*-parameters for the two phases for the parent and intergrowth samples. The *c*-parameter in the Gd-domain slightly contracts by 0.4% for the intergrowth. In contrast, the Ta-domain expands by about 1.4% for the intergrowth. This behavior indicates that the Ta-domain is impacted more by intergrowth formation than the Gd-domain, with the summary of lattice parameters after refinement in **Tables S2** and **S3**. This phenomenon occurs due to the lattice mismatch between the Bi_4TaO_8Cl and Bi_2GdO_4Cl layers and causes lattice distortion in the intergrowths. To investigate this effect on photocatalytic properties, the results from Williamson-Hall strain analysis is discussed in Section 3.3.

As discussed in the introduction, neutron powder diffraction experiments by Bhat *et al.* were able to detect changes in the Ta–O–Ta bond angles of Bi_4TaO_8Cl due to disorder introduced in the structure upon reducing crystallite size into the nanoscale regime.[29] In our study, we employed TS using synchrotron X-rays rather than neutrons as Gd shows high neutron absorption. The resulting X-ray PDF is dominated by the heavy metals due to the interaction between X-rays and the electrons comprising the material. However, as seen in **Figure 1b** and further highlighted in **Figures S1**, we were able to detect the Ta–O and Gd–O signals at 1.98 Å and 2.32 Å, respectively, even though the PDF was dominated by intense metal–metal peaks (**Tables S4-S9** contain supplementary PDF refinement results). As expected, the PDF of the 50% intergrowth sample reveals a broad peak at 2.2 Å as compared to Ta 0% or Ta 100% (**Figure S1b**). The broad peak can be described as a linear combination of the Gd–O and Ta–O bond lengths arising from intergrowth formation. To accommodate for the variation of lattice parameters induced by the intergrowth, anisotropic thermal displacement of the metals and oxygen atoms were included in the refinement, alongside refinement of the metal positions.

Changes in the M–O–M bond angles and degree of octahedral tilting have previously been identified as important structural features contributing to the photocatalytic activity of perovskite structures,[21,30,31] where M–O–M bond angles closer to linearity (180°) were associated with superior photocatalytic activity.[21] Thus, we examined the M–O–M bond angles to provide deeper insights into the observed photocatalytic properties of the intergrowth materials.[16] The bond angle investigated is illustrated in **Figure S2**, while the relevant bond angles are summarized in **Table 1**. The Ta–O–Ta bond angles follow the trend of Ta 50% (162.08°) > Ta 75% (159.29°) > Ta 25% (158.42°) among the intergrowths. Interestingly, we previously reported Ta 50% as the highest activity intergrowth for the oxygen evolution reaction (OER), which is consistent with the greater Ta–O–Ta bond angle leading to greater delocalization of the excitons of the semiconductor.[32] This delocalization leads to greater mobility of photogenerated electron-hole pairs, increasing the probability of electrons and holes to reach active sites on the surface of the photocatalyst. As the crystal structure of Bi_2GdO_4Cl does not consist of metal octahedral geometry, the Gd–O–Gd bond angle was largely conserved in the samples. Similar experimental OER activities were reported for Ta 25% and Ta 75%, while the Ta–O–Ta bond angle was just slightly less for Ta 25% compared to Ta 75%. The experimental OER activities for Ta 25% and Ta 75% do not perfectly correlate with respect to the Ta–O–Ta bond angles, being consistent with reduced charge carrier recombination as evident by photoluminescence measurements, and within the margin of error given their similar Ta–O–Ta bond angles and the sensitivity of OER activity to multiple variables.[16] We note that textural factors such as surface area could not account for the differences in photocatalytic activity as they were of comparable values.[16]

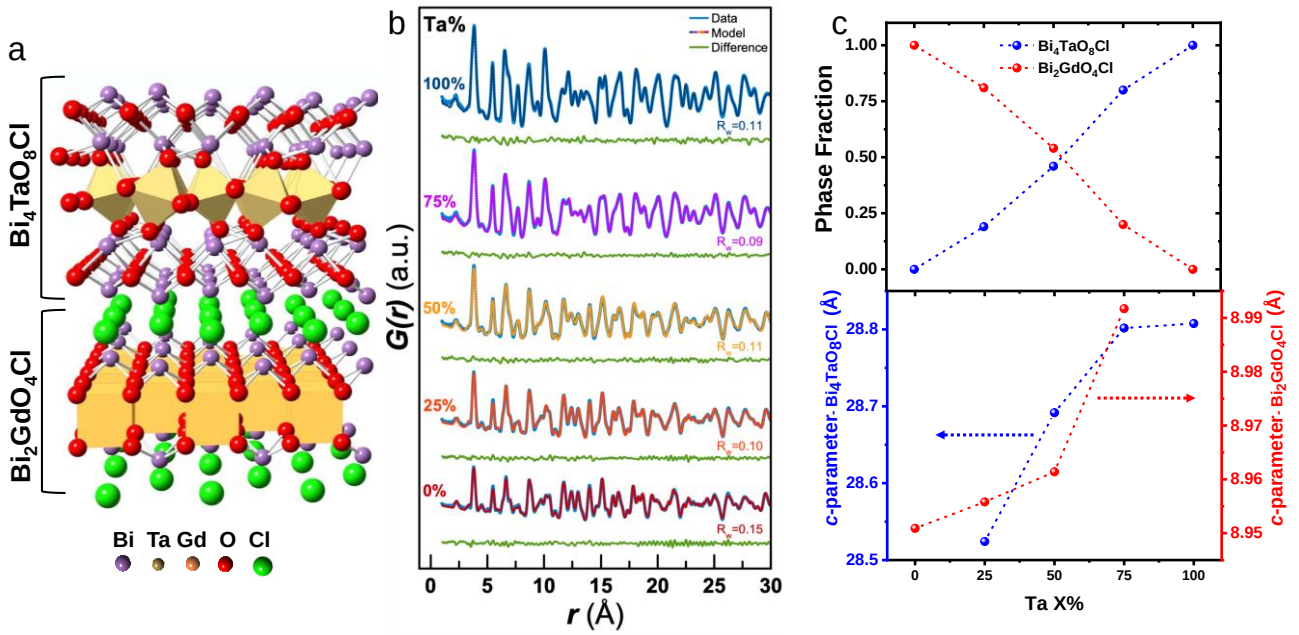

Figure 1. (a) Structure model of Bi_4TaO_8Cl-Bi_2GdO_4Cl intergrowth, where Ta:Gd is 1:1; an ordered structure is depicted to clearly present the building block layers but the actual intergrowths are disordered. (b) PDF refinement of Ta 100%, Ta 75%, Ta 50%, Ta 25%, and Ta 0%. (c) Results from the PDF refinement showing (top) the relative phase fractions and (bottom) the evolution in the *c*-parameter.

Table 1. Metal–O–Metal bond angle, band gaps and OER activities for the different samples.

Sample	Bi_4TaO_8Cl (°) [a]	$[TaO_6]$ Tilt (°)[b]	Bi_2GdO_4Cl (°)	Band Gap (eV)	OER Activity (μmol h^{-1})
Ta 0%	-	-	108.18	2.34	0.4
Ta 25%	158.42	1.91	107.99	2.38	1.0
Ta 50%	162.08	1.92	108.26	2.41	1.6
Ta 75%	159.29	1.95	108.21	2.45	0.9
Ta 100%	157.68	2.40	-	2.48	0.6

[a] M–O–M bond angle for Ta domain was calculated for the Ta–O–Ta bond in x-y direction. [b] Tilt was calculated for the $[TaO_6]$ octahedra present in Bi_4TaO_8Cl domain for all the intergrowths in the x-y direction. Band gap and OER activity were reported in reference 16, along with the primary data.

Another structural parameter which affects properties in all perovskite structures is the tilting of the metal octahedra.[33–35] The tilting of the octahedra impacts the optical absorption of semiconductors and has been studied extensively in halide perovskite systems.[36] Greater octahedral tilting reduces metal-anion orbital overlap, moving the bands to deeper energies and increasing the band gap of the material.[22] In order to investigate such effects in our system, we calculated the octahedral tilting in the intergrowth systems. We focused on the $[TaO_6]$ octahedra in the intergrowth systems as the Bi_2GdO_4Cl block does not have a perovskite-like structure and the Gd coordination environment is rigid to undergo any tilting or distortion. The tilt angle was calculated in the *x-y* direction as migration of charge carriers occurs in that direction for oppositely charged layered materials (see **Figure S2b**).[34,37,38] **Table 1** summarizes the tilt angle calculated for the intergrowth systems. Interestingly, this trend is the same as the band gaps of the samples estimated experimentally by UV-Visible Diffuse Reflectance Spectroscopy (UV-Vis DRS), which were 2.34, 2.38, 2.41, 2.45 and 2.48 eV for the Ta 0, 25, 50, 75 and 100% samples, respectively. This trend was corroborated with the band gap trend from density functional theory,[16] but the structural origin of this trend was unclear. The effect of tilting of the metal octahedra on the electronic structure originates from the constituent orbitals that form the band edges in perovskite systems.[22] In our case, the valence band edges (VBEs) of the intergrowths are composed of hybridized Bi–O orbitals, while in the conduction band edges (CBEs) are significantly hybridized Ta–O orbitals. Thus, lowering the tilt in the octahedra allows for greater orbital overlap between Ta–O orbitals in the CBE. This condition leads to a smaller band gap owing to the decreased anti-bonding character of the Ta–O bonds that reduces the energy of the CBE while the VBE stays almost constant. Further, in our previous report we observed localized atomic displacements via scanning transmission electron microscopy and we suspected them to be arising from changes in the Ta–O octahedral tilting and rotation.[16] Using X-ray TS and PDF analysis in this study, we can rationalize the origin of such displacements. Thus, through this local structure analysis study, we find that as the Ta–O–Ta bond angle of the metal octahedra tend towards linearity in the intergrowths, greater photocatalytic performance is achieved. Further, the degree of tilting of the metal octahedra correlates to the optical absorption property of the intergrowth material. Thus, the findings in this study can be expanded to design a library of intergrowths or related layered systems with tailored catalytic performance and optical properties.

3.2 Structure Mining

The order of layers in a layered crystal structure is crucial for charge carrier migration and transfer. For example, in tantalum-based Dion–Jacobson layered perovskites, the exchangeability of interlayer K^+ has an important influence on the photocatalytic activity towards the hydrogen evolution reaction. Even though the chemical properties of two-layer $KLaTa_2O_7$ and three-layer $KCa_2Ta_3O_{10}$ were similar, the photocatalytic activity of $KLaTa_2O_7$ was found to be two times higher than that of $KCa_2Ta_3O_{10}$.[39] Also, Sillén–Aurivillius layered oxyhalides with single-, double- and triple-perovskite slabs were found to be promising visible-light-driven photocatalysts for water splitting, with different behaviors observed depending on the number of perovskite blocks.[15] Altering the stacking in these oxyhalide systems causes changes in the internal electric field, leading to modulation of charge carrier migration. As these examples illustrate, quantifying the degree of disorder in the stacking sequence of a layered material is important to understanding how local structure influences properties and can be engineered toward greater performance.

Considering our Bi_4TaO_8Cl–Bi_2GdO_4Cl intergrowths, we previously reported Urbach tailing in the optical absorption spectra of the samples.[16] Such phenomenon arise from structural defects such as stacking faults, which are quite similar to what has been observed in other intergrowths. Thus, our approach to modeling the local structure of these materials must consider such occurrences to which several strategies have been developed. One approach, which is used in DiFFaX,[40] DiFFaX+,[41] and more recently implemented as the program FAULT in the FullProf suite[42] or in Topas[28,43,44] consists in modelling the PXRD pattern of a faulted crystal structure based on asymmetric units and a set of stacking probabilities. In these cases, the stacking probabilities indicating the amount of disorder in the structure can be refined. Another approach comprises of building supercells of the crystal structure, for example supercells of zeolites SAPO-18 and 34[45] or of $Ag_3LiIr_2O_6$[46] allowed stacking disorder to be incorporated.

By comparing model to experimentally obtained scattering data, planar faults were characterized and revealed their effect on the PXRD patterns. In this work, we combine these two approaches in a structure mining approach, developed in a previous paper.[27] A whole catalogue of supercells of intergrown Bi_4TaO_8Cl and Bi_2GdO_4Cl domains with varying amounts of Ta and Gd, as well as of disorder, are refined onto experimental datasets. The comparison of the goodness of fit between each supercell provides information on the microstructure of the

sample, giving guidance for the future design of new intergrowth photocatalysts.

To investigate the degree of disorder in the layered crystal structure of the intergrowths, supercells containing various amounts of each parent phase were modeled and refined on the experimental PXRD patterns. We recently used a similar approach for characterization of stacking disorder in γ-MnO_2.[27] γ-MnO_2 is an intergrowth of two parent structures, pyrolusite β-MnO_2 and ramsdellite R-MnO_2. γ-MnO_2 structures can thus be considered built through stacking of two types of building blocks:[47] [MnO_6] octahedra belonging to a pyrolusite domain and [MnO_6] octahedra of γ-MnO_2 belonging to a ramsdellite domain. Their sequence in the structure can be defined by a set of two probabilities, which allow for the wide diversity of intergrowth structures in γ-MnO_2 and estimation of the volume fraction of each phase in the intergrowth structure as well.[47]

Using a similar approach, we built Bi_4TaO_8Cl–Bi_2GdO_4Cl intergrowth *P*1 supercells. The first step was to extract units of each parent structure - a single layer of Bi_4TaO_8Cl (Ta-domain) and a single layer of Bi_2GdO_4Cl (Gd-domain) were extracted. For the Ta-domain, we extracted the unit from the low symmetry phase ($P2_1cn$), where distortions occur in the [TaO_6] octahedra layer. Because of these distortions of the [TaO_6] octahedra layers, two separate units were extracted, here named Ta and Ta'-layers, as described further below. Once the coordinates of every atom in the single layer were extracted, they were normalized so they shared a common origin, which was placed on the Bi atom. Furthermore, the Ta-domains underwent a rotation of 45° for them to match the orientation of atoms in the Gd-domain.

Once the units were extracted, they were stacked in an iterative way based on the set of probabilities: P_g and P_t. P_g refers to the probability of stacking of two Gd-domain layers one above the other, and P_t refers to the probability of stacking two Ta-domain layers one above the other, as presented in **Figure 2**. For each superstructure created a set of P_g and P_t values were fixed. The first layer in the structure was chosen randomly and, based on its nature (either Ta- or Gd-layer), the next layer was chosen according to the value of P_g (if it was a Gd-layer) or P_t (for a Ta-layer), which were fixed. A random number between 0 and 1 was generated and if its value was below P_g or P_t, a layer of the same type was stacked on top of it, or in the other case, a layer of the other type was stacked. The same process was carried out considering now the nature of the new layer, generating a new random number and comparing it to P_g and P_t again. Note that when two Ta-layers were stacked on top of each other, the second layer was the mirror reflection of the first Ta-layer (Ta'-layer). The process was iterated until 50 layers were stacked.

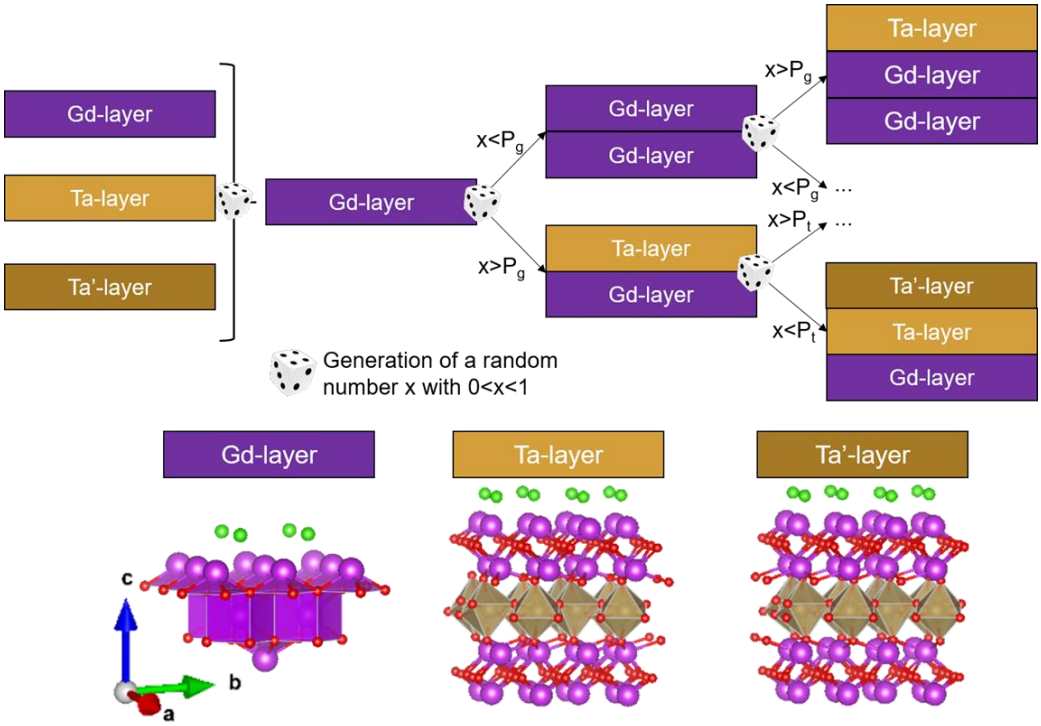

Figure 2: Summary of the supercell building process. A first layer was chosen randomly between a Gd-, a Ta-layer and its mirror Ta'-layer (shown at bottom). The stacking of the next layer depends on whether the randomly generated number between 0 and 1 was smaller or bigger than the value of P_g or P_t related to the previous layer. The process was repeated 50 times, following the same procedure.

Supercells with 50 layers were created for a whole range of (P_g, P_t) sets, varying P_g and P_t between 0.50 and 0.99 with an increment of 0.01, thus yielding 2500 supercells. Refinements using each supercell as a model was then carried out on the experimental PXRD patterns of samples Ta 75%, Ta 50% and Ta 25% (best fit refinements shown in **Figure S3**). The cell lattice parameters, thermal atomic displacement parameters,

background (fitted with Chebyshev polynomials) and TCHZ peak shape parameters were refined. The R_{wp} value of each Rietveld refinement, *i.e.,* the goodness of fit, was extracted and plotted as a function of the (P_g, P_t) set. Color maps for the structure mining results of each sample are shown in **Figure 3a-c**, where the colour represents the R_{wp} value. We observe for each

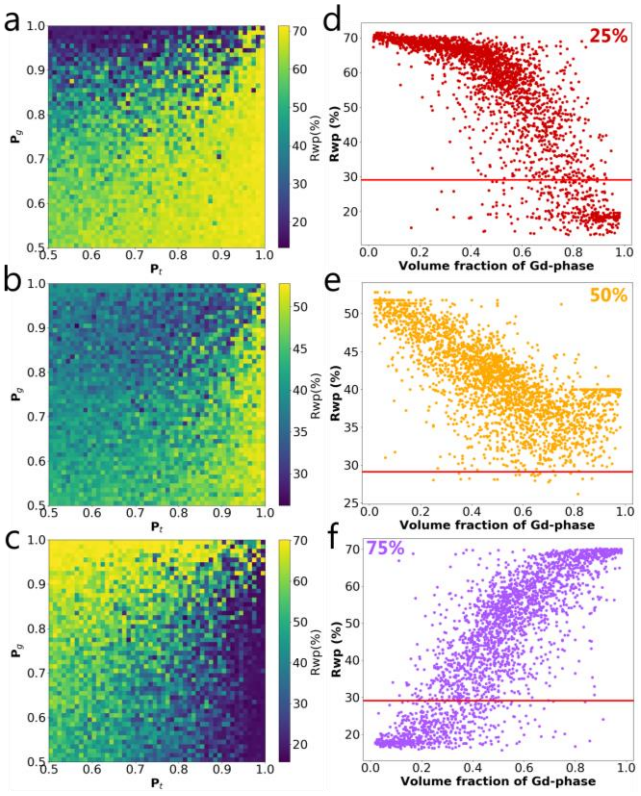

Figure 3: Plot of the R_{wp} value of the Rietveld refinements carried on (a) Ta 25%, (b) Ta 50% and (c) Ta 75% as a function of the (P_g, P_t) set of each supercell. R_{wp} value of the Rietveld refinements carried on sample (d) Ta 25%, (e) Ta 50% and (f) Ta 75% plotted as a function of the volume fraction of Gd-domain in each supercell. The R_{wp} value from the two-phase refinement of parent structures indicated by the vertical red line.

sample a dark-blue region systematically corresponding to a (P_g, P_t) range for which the fitting of the structure was better than the rest of the investigated (P_g, P_t) range. This trend can be better observed when the R_{wp} values are plotted as a function of the Gd-domain volume fraction shown in **Figure 3d-f**. The red line in the curve represents the fit quality obtained when using a simple two-phase model.

We can extract further statistical information from the refined mined structures by calculating the distribution of stacking probabilities P_g and P_t in a sample. To do so, the R_{wp} value of each superstructure refinement is plotted as a function of P_t and P_g as shown in **Figure S4-6(a, b)** for samples Ta 75%, Ta 50% and Ta 25% respectively. The average of the R_{wp} value for each P_g or P_t value is calculated and shown by the red curve on each plot. Because a high R_{wp} means a poor fit of the superstructure to the experimental data, and conversely and low R_{wp} value correspond to a good fit of the supercell, we assume that the average curve calculated above is representative of whether supercells with a given P_g or P_t value are representative of this goodness of fit. Hence, the inverse of that average curve is calculated and normalized so that the integrate of the obtained curve is equal to 1, giving thus a distribution of stacking probabilities P_t and P_g in a sample as shown in **Figure S4-6(c, d)** for samples Ta 75%, Ta 50% and Ta 25% respectively.

For Ta 75% (**Figure 3c,f**), the low-R_{wp} value area in (P_g, P_t) parameter space lies towards the high-P_t region, which is consistent with the fact that the sample contains a high fraction of Ta-domains. In Ta 75%, the distribution of Ta-domains stacking probability increases sharply at high P_t values, whereas the distribution of Gd-domains stacking probability falls as P_g tends towards 1 (**Figure S4**). This observation can be related to a distribution of large, segregated Ta-domains, separated by small Gd-domains. For Ta 50%, (**Figure 3b,e**) only a few supercells yielded a better fit than the two-phase refinement. The trends on these distributions of P_g and P_t observed for Ta 50% were opposite those observed for Ta 75%. This is an indication that Ta- and Gd-domains are separated from each other in Ta 50% in the supercell structure, corroborating our previous report via electron microscopy.[16,18]

When R_{wp} was plotted as a function of P_t and P_g individually in **Figure S5a,b** an opposite trend (P_t-increasing and P_g-decreasing) can be observed in the goodness of fit from structure mining of Ta 50% as shown in the orange curve. This observation supports that the intergrowth samples are forming a distribution of ordered Ta- and Gd-domains. In Ta 50%, the probability distribution of P_g exhibits a maximum when P_g tends toward 1, while the probability distribution of P_t shows a maximum below 0.85 and decreases sharply from there as P_t tends toward 1 (**Figure S5c,d**). This phenomenon indicates that the Gd-domains might be more ordered than the Ta-domains. Therefore, in Ta 50% the structure consists of large segregated Gd-domains separated by small Ta-domains. Finally, the opposite behavior occurs for Ta 25% as supercells with a high Gd-domain volume fraction yield the best fits (**Figure 3a,d**). For this sample, the distribution of P_t was high for P_t values tending towards 0.5, while the distribution of P_g increases when P_g tends toward 1, indicating large segregated Gd-domains, separated by a few layers of Ta-domain shown in **Figure S6**.

Interestingly, the Ta 25% and Ta 50% samples show the highest OER activity (**Table 1**), which could be related to the similar stacking fault distributions estimated above, where large Gd-domains are separated by narrower Ta-domains. The Ta 75% sample shows a higher OER activity than the parent phases, but not as high as the two other intergrowth samples. According to the results of the structure mining approach, the structure rather contains large Ta-domains separated by narrower Gd-domains. These findings suggest that an optimum in activity for the OER could be achieved by tailoring the distribution of Gd- and Ta- domains in the intergrowth structure, favoring segregated Gd-domains and scattered Ta-domains. It must be kept in mind that the structure mining process involved superstructures that extended up to 50 layers and thus

represents a mere "sampling" of the actual distribution of intergrowth in the different samples. The statistics of the distribution curves presented above could be improved by generating extended supercells but would require more computational power. We would also like to note that in our system we did not observe interchange of Ta and Gd from their respective crystallographic sites. This claim is corroborated by Scanning Transmission Electron Microscopy-Energy Dispersive X-ray Spectroscopy mapping for the Ta 50% intergrowth shown in **Figure S7** and also supported by our previous nanoscale investigation *via* atomically resolved electron microscopy.[18]

3.3 Strain analysis

In Section 3.1, we elucidated from PDF analysis that lattice strain exists at the interface between Bi_4TaO_8Cl and Bi_2GdO_4Cl layers and the degree depends on Ta content in accordance to related layered perovskite materials.[48–50] We observed the lattice *c*-parameter to be compressed for the Bi_4TaO_8Cl layer and elongated for the Bi_2GdO_4Cl layer. The strain can also occur due to the size of the coherently diffracting domains in the intergrowth, possibly leading to changes in optical absorption and charge carrier migration.[36] Strain induced in a photocatalyst is known to tailor the electronic structure and thereby can regulate the OER activity in perovskite systems by tuning the M–O chemisorption.[50,51]

the peak profile can be described by a Pseudo-Voigt function in order to extract peak position and width. For the PXRD patterns of the Ta 75%, Ta 50%, and Ta 25% samples, reflections from the two parent structures between 1.5 and 8.5° 2θ were modelled individually. Peak position and FWHM were extracted to build the WH plots by fitting a Pseudo-Voigt function to individual peaks. An example of peak fitting is shown in **Figure S8** where the (001) reflection of the Gd-domain and the (006) reflection of the Ta-domain in the XRD pattern of sample Ta 50% are fitted. Due to overlap of some reflections of the two parent structures, only peaks that were well separated were used for the analysis. The resulting WH plots of the Ta 75%, Ta 50% and Ta 25% samples consisting of Bi_4TaO_8Cl and Bi_2GdO_4Cl domains are shown in **Figure 4**. Linear trends could be established among (00*l*), (01*l*) and (11*l*) plane families and first-degree polynomials could be fitted. They are shown by solid lines in **Figure 4**.

Strain in lattice planes can be related to the slope of the linear regression. The slope denoted by η has been extracted for each domain and each family of lattice planes and are tabulated in **Table 2**. The R-square factors of each linear regression are summarized in **Table S10**. For the three samples investigated, regardless of the amount of each domain in the intergrowth sample and of the family of lattice planes, the amount of strain in the Ta-domain remains as seen in Table 2. The slope η for crystallographic planes of index (00*l*), (01*l*) and

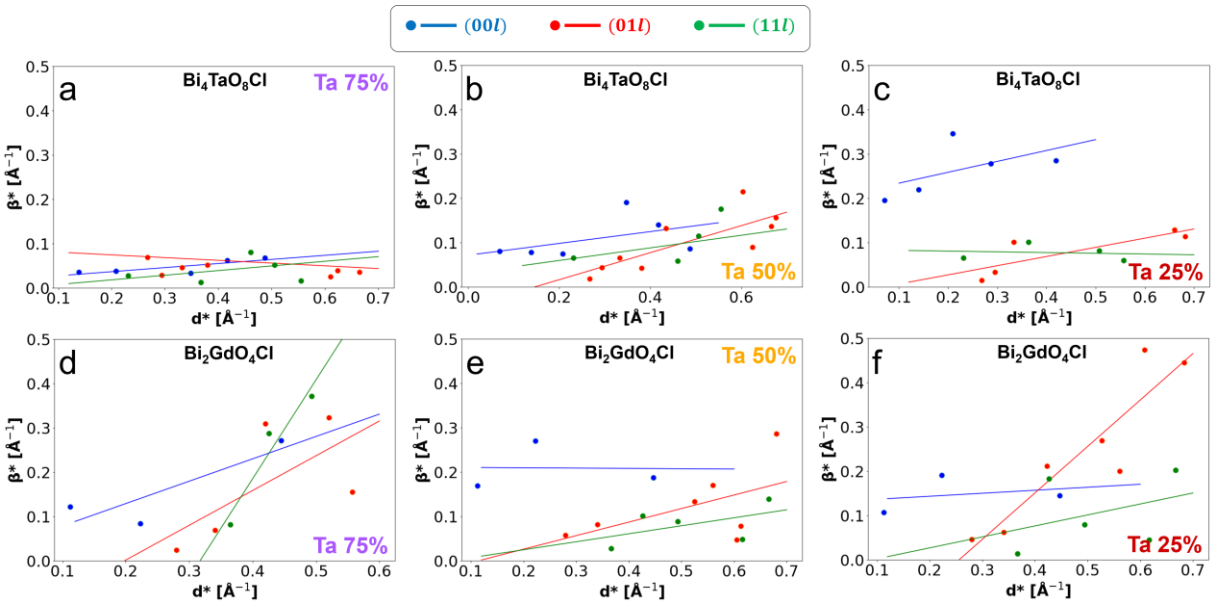

Figure 4: Williamson-Hall plots of the (00*l*) (blue dots), (01*l*) (red dots) and (11*l*) (green dots) reflections of Bi_4TaO_8Cl for samples (a) Ta 75%, (b) Ta 50% and (c) Ta 25%; and that of Bi_2GdO_4Cl were (d) Ta 75%, (e) Ta 50% and (f) Ta 25%. The linear trends related to size and strains effects for each family of planes were supported by a linear regression, shown by straight lines of the same color as the families of planes.

Thus, to investigate non-uniform strain in these systems, we carried out Williamson-Hall (WH) analysis.[52] The strain along different crystallographic directions of each layer were investigated using WH plots. Such plots assume that the Bragg peak broadening arising from strain and size can be separated from their dependence on the Bragg scattering angle, according to the Williamson-Hall equation.[52] We here further assume that

(11*l*) on the WH plots remains on average around 0.15, except for the Ta 50% sample for which the (01*l*) planes appear to have a greater amount of strain than in the other two samples. On the other hand, η for the Gd-domain is higher relative to the Ta-domains for the crystallographic planes of index (01*l*) and (11*l*) in the Ta 75%, Ta 50% and Ta 25% samples (Table 2). In Ta 50%, the slope of (01*l*) in each Ta- and Gd-domains is about 0.305,

indicating that in this particular sample, the amount of strain is shared in equal part between the two layers. We note here that few Williamson-Hall plots have trendlines that deviates from linearity. The origin of such non-linear behavior could be due to hkl-dependent interference phenomena in X-ray diffraction from adjacent nanocrystalline domains.[53] In our analysis we have assumed no effect of the interference phenomenon.

These observations indicate that in every sample, strains are situated in the Gd-domains. An explanation for this preference could be that the [TaO_6] octahedral planes in the Ta-domain have the ability to distort/tilt, which therefore dissipates the strain in the Ta-domains. On the other hand, the [GdO_8] units show more rigidity and, in turn, experience more strain. Recall, for Ta 50%, the Ta-domains are distributed more randomly compared to Ta 25% and Ta 75%. For that reason, the Ta-domains in Ta 50% may experience greater strain, corroborating our observation of larger broadening of the (002) reflections from Ta-domains of Ta 50% found in our previous report.[16] Significantly, development of greater strain in Ta 50% further corroborates its greater activity for the OER (Table1) among the intergrowths in accordance with literature reports.[54,55] Concerning the Gd-domains, the [GdO_8] cubic layers in a Gd-domain do not have the structural flexibility to tilt/distort, and the Gd-domain, thus, remains constrained in the intergrowth samples. These findings highlight how flexible and rigid layers can be selected to precisely tune the local structure of new intergrowths *via* strain engineering.

Table 2. Slope η of (00*l*), (01*l*) and (11*l*) lattice pane families in Ta- and Gd-domains for samples Ta 75%, 50% and 25%.

Sample	Ta-domain (00*l*)	Ta-domain (01*l*)	Ta-domain (11*l*)	Gd-domain (00*l*)	Gd-domain (01*l*)	Gd-domain (11*l*)
Ta 75%	0.0924	-0.0617	0.1048	0.5047	0.7846	2.2332
Ta 50%	0.1332	0.3051	0.1422	-0.0071	0.3052	0.1802
Ta 25%	0.2455	0.2069	-0.0165	0.0678	1.0485	0.2478

4. Conclusion

The local structures of Bi_4TaO_8Cl–Bi_2GdO_4Cl photocatalysts were analyzed by experimental X-ray TS and PDF analysis, along with Rietveld analysis of intergrowth supercells and Williamson-Hall plot analysis, to correlate metal coordination environments to photocatalytic performance. The greatest changes in lattice parameters were observed in the *c*-direction, where the Ta-domains shrunk and Gd-domains expanded with intergrowth formation due to lattice mismatch at the interface between Bi_4TaO_8Cl and Bi_2GdO_4Cl layers. Experimentally obtained photocatalytic performance correlated with changes in the Ta-domains, where greater photocatalytic performance was associated with greater linearity of the Ta–O–Ta bond angle and greater tilting of the [TaO_6] octahedra was associated with a larger band gap.

Structure mining analysis from experimental PXRD was used to model the intergrowths, revealing that the Ta- and Gd-domains are separated among each other, with large Gd-domains separated by small Ta-domains at high Gd% and the inverse for high Ta%. WH analysis found that the Gd-domains experienced greater strain compared to Ta-domains. The reason could be due to the rigidity of the [GdO_8] cubic layer relative to the structural flexibility of the [TaO_6] octahedral layers, which can distort/tilt. Thus, the [TaO_6] dissipates the strain in the Ta-domains that may build up at the interface between a Ta- and a Gd-domains due to unit cell mismatch. In particular, Ta 50% experienced greater strain compared to other intergrowths. And thereby led to greater photocatalytic activity of Ta 50% towards OER compared to the other intergrowths.

Overall, these findings highlight that strain engineering through the selection of rigid and flexible intergrowth layers is a promising pathway to modulate the local structure of materials toward efficient photocatalysis. Further, our studies correlate local structure to catalytic activity, enabling greater design of future photocatalytic materials.

Conflicts of interest

There are no conflicts to declare.

Acknowledgements

This work used funding support for K.C., and S.E.S. from US NSF DMR SSMC 2113536 and Indiana University. Access to the powder diffractometer was provided by NSF CRIF CHE 1048613. We also want to thank the IU Electron Microscopy Center and Nanoscale Characterization Facility for access to the necessary instrumentation. K.C. acknowledges the Raymond Siedle Fellowship and Carroll Family Fellowship support from Dept. of Chemistry, Indiana University. K.C. is grateful to Matthew N. Gordon, Nayana C.B. and Jack S. Googasian for helpful discussions. K.M.Ø.J and J.K.M. are grateful to the Villum Foundation for financial support through a Villum Young Investigator grant (VKR00015416). Funding from the Danish Ministry of Higher Education and Science through the SMART Lighthouse is gratefully acknowledged.

Author Contributions

K.C. and S.E.S. conceived the project. K.C. synthesized the samples and performed the photocatalytic and band gap measurements. J.K.M. performed synchrotron beamline experiments and PDF refinements. N.P.L.M. performed the structure mining calculations and WH analysis. K.C., J.K.M. and N.P.L.M. analysed the results. K.C. and S.E.S. wrote the manuscript with inputs from all authors. K.M.Ø.J. and S.E.S. supervised the project.

References

1 Q. Wang and K. Domen, *Chem. Rev.*, 2020, **120**, 919–985.
2 F. E. Osterloh, *Chem. Soc. Rev.*, 2013, **42**, 2294–2320.
3 L. F. Bobadilla, J. L. Santos, S. Ivanova, J. A. Odriozola and A. Urakawa, *ACS Catal.*, 2018, **8**, 7455–7467.
4 Y. Chen, C. Yan, J. Dong, W. Zhou, F. Rosei, Y. Feng and L.-N. Wang, *Adv. Funct. Mater.*, 2021, **31**, 2104099.
5 A. Vega-Peñaloza, J. Mateos, X. Companyó, M. Escudero-Casao and L. Dell'Amico, *Angew. Chem., Int. Ed.*, 2021, **60**, 1082–1097.
6 R. Chen, F. Fan, T. Dittrich and C. Li, *Chem. Soc. Rev.*, 2018, **47**, 8238–8262.
7 L. Lin, T. Hisatomi, S. Chen, T. Takata and K. Domen, *Trends Chem.*, 2020, **2**, 813–824.
8 D. P. Chen, J. C. Neuefeind, K. M. Koczkur, D. L. Bish and S. E. Skrabalak, *Chem. Mater.*, 2017, **29**, 6525–6535.
9 K. Chatterjee and S. E. Skrabalak, *ACS Appl. Mater. Interfaces*, 2021, **13**, 36670–36678.
10 D. Abeysinghe and S. E. Skrabalak, *ACS Energy Lett.*, 2018, **3**, 1331–1344.
11 H. Fujito, H. Kunioku, D. Kato, H. Suzuki, M. Higashi, H. Kageyama and R. Abe, *J. Am. Chem. Soc.*, 2016, **138**, 2082–2085.
12 K. Chatterjee, M. Banoo, S. Mondal, L. Sahoo and U. K. Gautam, *Dalton Trans.*, 2019, **48**, 7110–7116.
13 X. Tao, Y. Zhao, L. Mu, S. Wang, R. Li and C. Li, *Adv. Energy Mater.*, 2018, **8**, 1701392.
14 D. Kato, K. Hongo, R. Maezono, M. Higashi, H. Kunioku, M. Yabuuchi, H. Suzuki, H. Okajima, C. Zhong, K. Nakano, R. Abe and H. Kageyama, *J. Am. Chem. Soc.*, 2017, **139**, 18725–18731.
15 D. Ozaki, H. Suzuki, K. Ogawa, R. Sakamoto, Y. Inaguma, K. Nakashima, O. Tomita, H. Kageyama and R. Abe, *J. Mater. Chem. A*, 2021, **9**, 8332–8340.
16 K. Chatterjee, R. Dos Reis, J. K. Harada, J. K. Mathiesen, S. L. A. Bueno, K. M. Ø. Jensen, J. M. Rondinelli, V. Dravid and S. E. Skrabalak, *Chem. Mater.*, 2021, **33**, 347–358.
17 A. M. Kusainova, W. Zhou, J. T. S. Irvine and P. Lightfoot, *J. Solid State Chem.*, 2002, **166**, 148–157.
18 K. Chatterjee, S. Bueno, S. Skrabalak, V. Dravid and R. dos Reis, *Microsc. Microanal.*, 2020, **26**, 376-379.
19 C. N. R. Rao, *Bull. Mater. Sci.*, 1985, **7**, 155–178.
20 C. N. R. Rao and J. M. Thomas, *Acc. Chem. Res.*, 1985, **18**, 113–119.
21 A. Kudo, H. Kato and S. Nakagawa, *J. Phys. Chem. B*, 2000, **104**, 571–575.
22 S. Balaz, S. H. Porter, P. M. Woodward and L. J. Brillson, *Chem. Mater.*, 2013, **25**, 3337–3343.
23 A. P. Hammersley, S. O. Svensson, M. Hanfland, A. N. Fitch and D. Hausermann, *High Pressure Res.*, 1996, **14**, 235–248.
24 A. P. Hammersley, *J. Appl. Crystallogr.*, 2016, **49**, 646–652.
25 X. Yang, P. Juhas, C. L. Farrow and S. J. L. Billinge, *arXiv,* 2015*, preprint, arXiv:1402.3163, https://arxiv.org/abs/1402.3163v3.*
26 C. L. Farrow, P. Juhas, J. W. Liu, D. Bryndin, E. S. Božin, J. Bloch, T. Proffen and S. J. L. Billinge, *J. Phys.: Condens. Matter*, 2007, **19**, 335219.
27 N. Magnard, A. S. Anker, A. Kirsch and K. M. Ø. Jensen, *ChemRxiv,* 2022*, preprint, DOI:10.26434/chemrxiv-2022-rk7tp.v1.*
28 A. A. Coelho, *J. Appl. Crystallogr.*, 2018, **51**, 210–218.
29 S. S. M. Bhat, D. Swain, M. Feygenson, J. C. Neuefeind, A. K. Mishra, J. L. Hodala, C. Narayana, G. V. Shanbhag and N. G. Sundaram, *Inorg. Chem.*, 2017, **56**, 5525–5536.
30 G. Blasse, *J. Solid State Chem.*, 1988, **72**, 72–79.
31 G. Blasse and L. H. Brixner, *Mater. Res. Bull.*, 1989, **24**, 363–366.
32 H. Kato and A. Kudo, *J. Phys. Chem. B*, 2001, **105**, 4285–4292.
33 A. M. Abakumov, R. Erni, A. A. Tsirlin, M. D. Rossell, D. Batuk, G. Nénert and G. V. Tendeloo, *Chem. Mater.*, 2013, **25**, 2670–2683.
34 W. Lu, W. Dong Song, K. He, J. Chai, C.-J. Sun, G.-M. Chow and J.-S. Chen, *J. Appl. Phys.*, 2013, **113**, 063901.
35 K. T. Butler, *J. Mater. Chem. C*, 2018, **6**, 12045–12051.
36 R. Prasanna, A. Gold-Parker, T. Leijtens, B. Conings, A. Babayigit, H.-G. Boyen, M. F. Toney and M. D. McGehee, *J. Am. Chem. Soc.*, 2017, **139**, 11117–11124.
37 H. J. Xiang, M. Guennou, J. Íñiguez, J. Kreisel and L. Bellaiche, *Phys. Rev. B*, 2017, **96**, 054102.
38 J. He, A. Borisevich, S. V. Kalinin, S. J. Pennycook and S. T. Pantelides, *Phys. Rev. Lett.*, 2010, **105**, 227203.
39 P. Wang, W. Chen, Z. Wang, Y. Tang, W. Shi and L. Tang, *Dalton Trans.*, 2021, **50**, 16076–16083.
40 M. M. J. Treacy, J. M. Newsam and M. W. Deem, *Proc. R. Soc. London, Ser. A*, 1991, **433**, 499–520.
41 M. Leoni, A. F. Gualtieri and N. Roveri, *J. Appl. Crystallogr.*, 2004, **37**, 166–173.
42 M. Casas-Cabanas, M. Reynaud, J. Rikarte, P. Horbach and J. Rodríguez-Carvajal, *J. Appl. Crystallogr.*, 2016, **49**, 2259–2269.
43 C. M. Ainsworth, J. W. Lewis, C.-H. Wang, A. A. Coelho, H. E. Johnston, H. E. A. Brand and J. S. O. Evans, *Chem. Mater.*, 2016, **28**, 3184–3195.
44 A. A. Coelho, J. S. O. Evans and J. W. Lewis, *J. Appl. Crystallogr.*, 2016, **49**, 1740–1749.
45 W. A. Sławiński, D. S. Wragg, D. Akporiaye and H. Fjellvåg, *Microporous Mesoporous Mater.*, 2014, **195**, 311–318.
46 S. Bette, T. Takayama, V. Duppel, A. Poulain, H. Takagi and R. E. Dinnebier, *Dalton Trans.*, 2019, **48**, 9250–9259.
47 Y. Chabre and J. Pannetier, *Prog. Solid State Chem.*, 1995, **23**, 1–130.
48 M. Luo and S. Guo, *Nat. Rev. Mater.*, 2017, **2**, 1–13.
49 Y. Chen, Y. Lei, Y. Li, Y. Yu, J. Cai, M.-H. Chiu, R. Rao, Y. Gu, C. Wang, W. Choi, H. Hu, C. Wang, Y. Li, J. Song, J. Zhang, B. Qi, M. Lin, Z. Zhang, A. E. Islam, B. Maruyama, S. Dayeh, L.-J. Li, K. Yang, Y.-H. Lo and S. Xu, *Nature*, 2020, **577**, 209–215.
50 Y. Miao, Y. Zhao, S. Zhang, R. Shi and T. Zhang, *Adv. Mater.*, 2022, **34**, 2200868.
51 B. You, M. T. Tang, C. Tsai, F. Abild-Pedersen, X. Zheng and H. Li, *Adv. Mater.*, 2019, **31**, 1807001.
52 G. K. Williamson and W. H. Hall, *Acta Metall.*, 1953, **1**, 22–31.
53 D. Rafaja, V. Klemm, G. Schreiber, M. Knapp and R. Kužel, *J. Appl. Crystallogr.*, 2004, **37**, 613–620.
54 A. E. Maegli, S. Pokrant, T. Hisatomi, M. Trottmann, K. Domen and A. Weidenkaff, *J. Phys. Chem. C*, 2014, **118**, 16344–16351.
55 D. Dai, X. Liang, B. Zhang, Y. Wang, Q. Wu, X. Bao, Z. Wang, Z. Zheng, H. Cheng, Y. Dai, B. Huang and P. Wang, *Adv. Sci.*, 2022, **9**, 2105299.